

Provided for non-commercial research and educational use only.
Not for reproduction or distribution or commercial use.



HYPERVELOCITY IMPACT
PROCEEDINGS OF THE 2005 SYMPOSIUM

Lake Tahoe, California
9-13 October 2005

Guest Editor
WILLIAM P. SCHONBERG



This article was originally published in a journal published by Elsevier, and the attached copy is provided by Elsevier for the author's benefit and for the benefit of the author's institution, for non-commercial research and educational use including without limitation use in instruction at your institution, sending it to specific colleagues that you know, and providing a copy to your institution's administrator.

All other uses, reproduction and distribution, including without limitation commercial reprints, selling or licensing copies or access, or posting on open internet sites, your personal or institution's website or repository, are prohibited. For exceptions, permission may be sought for such use through Elsevier's permissions site at:

<http://www.elsevier.com/locate/permissionusematerial>



ELSEVIER

Available online at www.sciencedirect.com

ScienceDirect

International Journal of Impact Engineering 33 (2006) 625–633

INTERNATIONAL
JOURNAL OF
**IMPACT
ENGINEERING**

www.elsevier.com/locate/ijimpeng

Hypervelocity impact modeling with different equations of state

M.E. Povarnitsyn*, K.V. Khishchenko, P.R. Levashov

Institute for High Energy Densities, Russian Academy of Sciences, Izhorskaya Street 13/19, 125412 Moscow, Russia

Available online 13 November 2006

Abstract

This study focuses on the simulation of hypervelocity impact problems with different equations of state (EOSs). We used a high-order multi-material Godunov method in Eulerian form and applied an “exact” multi-material Riemann solver to find more accurate individual phase advection fluxes regardless of the aggregate state. We investigated effects of melting in strong shock waves, evaporation in rarefaction waves and spallation. We found that a careful treatment of the spall formation mechanism is of greatest importance in obtaining accurate numerical results. Three types of wide-range EOSs are discussed—caloric EOS in unified analytical form for condensed and rarefied matter; thermodynamically complete stable multi-phase EOS in tabular form which does not allow for metastable states; and thermodynamically complete metastable EOS in tabular form which permits metastable gas, liquid or solid phases.

© 2006 Elsevier Ltd. All rights reserved.

Keywords: Spallation; Fragmentation; Equation of state; Aluminum; Lead

1. Introduction

The ability of multi-material Eulerian methods to handle arbitrarily large deformation and the generation of new free surfaces makes them attractive for problems of hypervelocity impact and penetration. These phenomena may often be described in terms of high-pressure physics ($P > 1$ Mbar). This limitation makes the deviatoric stress components much smaller than the pressure so that deviatoric stresses may be ignored, at least for early event times. Therefore, some hydrocodes treat all materials as inviscid fluids and the evaluation of mean pressure in a multi-material cell is based on the classical mixture theory for ideal fluids found in thermodynamics. Application of such codes is justified in modeling of accident scenarios associated with spacecraft shielding or safety-related problems in nuclear energy production. Impact loading of plate targets by impactors is extensively discussed in the review articles [1,2].

One of the fundamental problems in multi-material physics is the numerical treatment of interfaces. In a typical case, an interface separates two nonmixing materials and numerical calculation may introduce some smearing and artificial mixing of the components. For the validity and quality of the numerical simulation, it is essential to resolve interfaces with a proper accuracy.

Early hydrocodes have dealt with gases and since then a considerable success in treatment of condensed materials in wide range of parameters has been achieved. One should keep in mind the important difference

*Corresponding author. Tel.: +7 495 4842456; fax: +7 495 4857990.

E-mail address: povar@ihed.ras.ru (M.E. Povarnitsyn).

between condensed matter and gas physics and that is the ability of solids and fluids to sustain negative pressure. A complication arises in the case of spallation when the pressure drops below the dynamical tensile strength. This difficulty may be overcome by introduction of a fragmentation model into the numerical scheme. Dynamical strength basically is a function of many parameters (time, velocity, temperature, density, etc.) and the physics that governs the fragmentation process is not entirely understood. Models of spall growth under different loading conditions are discussed in [3,4].

2. Method

Our original numerical method is based on a conservative high-order multi-material Godunov approach in Eulerian form [5] and admits the usage of arbitrary equation of state (EOS). We model multiple phases by constructing an effective single phase in which the density, specific energy, and elastic properties are given by self-consistent averages of the individual phase properties, including their relative abundances. Following the ideas of Henderson et al. [6], we construct an effective single phase by holding the entropies of each phase constant during compression giving an expression for the isentropic bulk modulus of the mixture:

$$\bar{K}_S = \left[\sum_{\alpha} f_{\alpha} / K_{\alpha} \right]^{-1}, \quad (1)$$

where f_{α} and K_{α} denote the volume fraction and isentropic bulk modulus of component α , respectively. The entropy of each phase may be held individually constant because thermal equilibrium cannot be maintained on the scales of length and time, which we used in our experiments. For instance, the time scale for thermal diffusion is of order L^2/k , where L is the length scale and k is the thermal diffusivity. The time scale for pressure equalization is of order L/c , where c is the sound speed. In condensed matter the thermal diffusivity and sound speed are typically of order $10^{-6} \text{ m}^2/\text{s}$ and 10^3 m/s , respectively and thus, processes become comparable for length scales on the order of 10^{-9} m , a few orders smaller than our typical computational cell size.

We used a piecewise linear interpolation of primitive variables with the slope limiter of van Leer [7] together with an upwind characteristic tracing method [8], which makes our scheme second-order by space and time in zones of smooth flow. We used a second-order volume-of-fluid interface reconstruction algorithm [9] to decompose the effective single-phase fluxes back into the appropriate individual component phase quantities. Possible cavitation of material under negative pressures is controlled by the model of instant fragmentation. There are several criteria of spall formation incorporated into our numerical method. First of all, we control

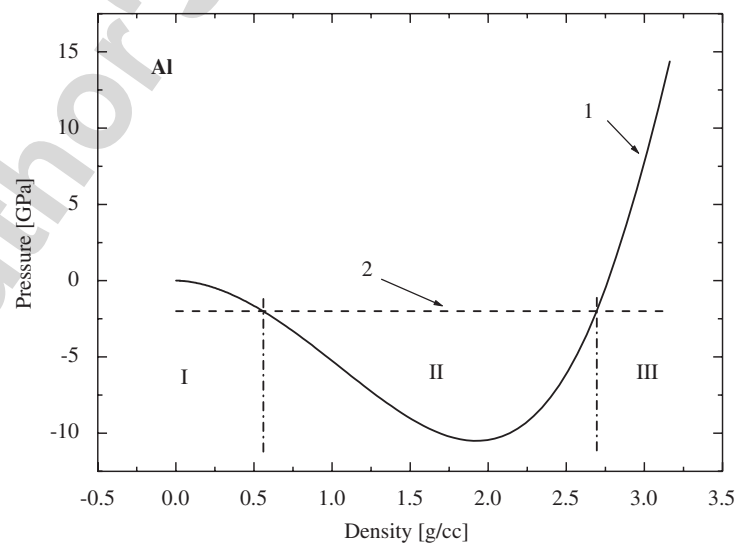


Fig. 1. Cold curve of aluminum (1) together with model dynamical tensile strength (2). Possible pressure values are limited from below by cold curve in zones I and III and by dynamical tensile strength in zone II.

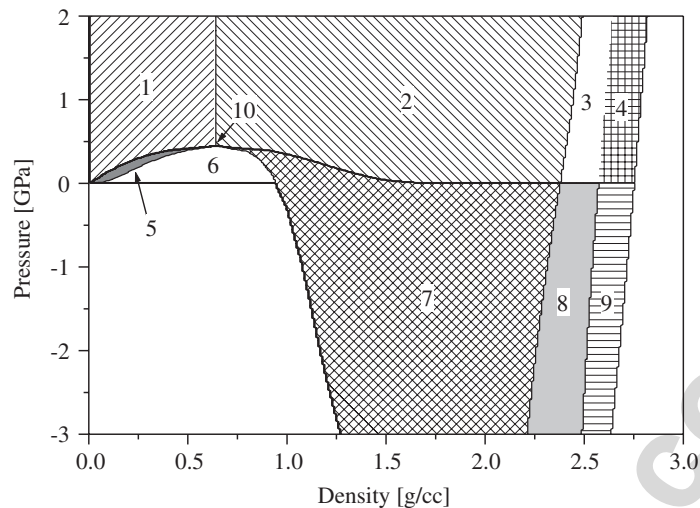


Fig. 2. Phase plane of the temperature complete metastable equation of state of aluminum. Phase states are as follows: gas (1), liquid (2), melting region (3), solid (4), metastable gas (5), stable liquid–gas mixture (6), metastable liquid (7), metastable solid–liquid mixture (8), and metastable solid (9). Boundary between phases (1) and (2) with the critical point (10) is conventional.

the moment of pressure drop below the dynamical tensile strength (constant in our experiments), Fig. 1. The second assumption is that none of the rarefaction waves may cross the cold curve, the position of which is known from the EOS, Fig. 1. For condensed fraction, the dynamical tensile strength limit is reached first (zone II in Fig. 1), whilst states of near liquid–gas or gas phases ($\rho < 0.5$ g/cc) are limited by the cold curve (zone I). Finally, the temperature complete metastable EOS provides us with information about the phase state of matter (Fig. 2) and we suppose that metastable liquid does not exist under negative pressure. If one of the discussed criteria is accomplished, vacuum is introduced into the computational cell and pressure is relaxed to zero value.

In some numerical experiments, we have found that use of wide-range EOSs requires accurate solution to the Riemann problem especially in the vicinity of phase transitions. Some Riemann solvers can give a very bad fit to the correct solution of the problem and result in undesirable oscillations and even unphysical states after the integration step. For this reason we used an “exact” multi-material Riemann solver that is quite expensive computationally but on the other hand gives the best possible solution regardless of the phase state under consideration. The extremely wide range of resolvable densities (almost ten orders) in our calculations is a justification of the “exact” solver usage, details of which will be discussed in the next section.

3. The Riemann problem

Solution to the Riemann problem is a backbone of any numerical method based on Godunov’s approach. The canonical Riemann problem is an initial value problem consisting of two constant left and right states with different velocities and pressures in juxtaposition. The solution of this problem is a set of waves with amplitudes chosen to satisfy appropriate interface compatibility conditions. Careful treatment of the Riemann problem makes the algorithm more accurate and robust. Unfortunately, this problem cannot be solved explicitly even in the case of ideal gas and thus several approximate approaches have been developed [8,10,11]. Acoustic approximation seems to be the simplest way to find the intersection point of left and right curves on the pressure particle velocity plane (P, U) and may be applicable to problems with weak discontinuities. It is well known that a surprisingly large number of condensed materials have a very simple linear relation between shock and particle velocities. Dukowicz [11] used this fact to construct a quadratic $P(U)$ function as an approximation of shock Hugoniot. Some materials are not well described by this assumption (especially near phase transitions). To overcome these difficulties, we use more general approach in the solution to the Riemann problem. It may be referenced as the “exact” solver and

accomplished by writing

$$U_L(P) = U_L - \begin{cases} \int_{P_L}^P \frac{(\bar{V}_L - \bar{V}) + (P_L - P)(d\bar{V}/dP)_H}{2\sqrt{(P - P_L)(\bar{V}_L - \bar{V})}} dP, & P > P_L \text{ (shock wave)} \\ \int_{P_L}^P \frac{1}{\sqrt{\bar{\rho}\bar{K}_S}} dP, & P < P_L \text{ (rarefaction wave)} \end{cases} \quad (2a)$$

$$U_R(P) = U_R + \begin{cases} \int_{P_R}^P \frac{(\bar{V}_R - \bar{V}) + (P_R - P)(d\bar{V}/dP)_H}{2\sqrt{(P - P_R)(\bar{V}_R - \bar{V})}} dP, & P > P_R \text{ (shock wave)} \\ \int_{P_R}^P \frac{1}{\sqrt{\bar{\rho}\bar{K}_S}} dP, & P < P_R \text{ (rarefaction wave)} \end{cases} \quad (2b)$$

where

$$(d\bar{V}/dP)_H = \frac{\bar{V} + (\bar{V} - \bar{V}_{L,R})\bar{\gamma}/2}{(P - P_{L,R})\bar{\gamma}/2 - \bar{K}_S} \quad (3)$$

is a derivative along the Hugoniot curve and $\bar{\gamma}$ is a thermodynamic Grüneisen parameter of the mixture. In these equations, the specific volume of the mixture

$$\bar{V} = \left[\sum_{\alpha} f_{\alpha}/V_{\alpha} \right]^{-1}, \quad (4)$$

isentropic bulk modulus \bar{K}_S , and Grüneisen parameter $\bar{\gamma}$ are available from the EOSs for each component.

In a multi-material computational cell, we should specify thermodynamic Grüneisen parameter of the mixture. The simplest model for calculation of this parameter is obtained by assuming that during isopycnic process, individual phase densities remain constant and there is no energy exchange between phases. Under these conditions one can derive

$$\bar{\gamma} = \left[\sum_{\alpha} f_{\alpha}/\gamma_{\alpha} \right]^{-1}. \quad (5)$$

We applied a fifth-order Runge–Kutta method to integrate system (2) to the common upper limit of integration P until the left-hand sides $U_L(P)$ and $U_R(P)$ are equal. Then, other thermodynamic variables under these conditions are known from the evaluation of corresponding integrands. For instance, during rarefaction of the mixture the individual phase density ρ_{α} and specific internal energy E_{α} of the component α are known from the following relations $\partial\rho_{\alpha}/\partial P = \rho_{\alpha}/K_{\alpha}$ and $\partial E_{\alpha}/\partial P = P/(\rho_{\alpha}K_{\alpha})$. Thus, all individual phase densities and specific energies can be calculated and then used in construction of individual fluxes.

4. The equations of state

We used three types of EOSs: caloric EOS for condensed and rarefied matter (EOS1), thermodynamically complete stable EOS in tabular form (EOS2) and thermodynamically complete metastable EOS in tabular form which permits the existence of metastable gas, liquid or solid phases (EOS3).

The semi-empirical caloric model of EOS1 [12] is defined by the dependence $E = E(P, \rho)$, which does not contain information about temperature and phase states of matter. The model generalizes the well-known Mie–Grüneisen EOS for the condensed phase and contains rather complex expressions for the cold curve (isotherm $T = 0$ K) and thermal part. The EOS1 model has correct asymptotic behavior at $\rho \rightarrow \infty$ (nonrelativistic ideal Fermi gas limit) and $\rho \rightarrow 0$ (classical ideal gas limit). The EOSs for aluminum and lead used in this work are in good agreement with experimental points on shock compression and adiabatic expansion even at tenfold expansion. Accurate representation of theoretical and experimental data gives rise to very similar simulation results for caloric and temperature complete EOSs (see below).

The semi-empirical multi-phase EOSs (EOS2, EOS3) are based on an earlier model of Bushman [13], which takes into account the effects of high-temperature melting and evaporation, and the possible existence of

metastable states including negative pressure range. This multi-phase EOS consistently describes the collection of experimental data on static and shock compression as well as adiabatic and isobaric expansion of metal.

The thermodynamic quantities were determined using a special interpolation procedure on tabular functions $f_{i,j} = f(\rho_i, T_j)$, where f is one of thermodynamic parameters (in our case, the internal energy E , the pressure P , the Grüneisen parameter γ , and the adiabatic sound velocity c).

In the stable case (EOS2), the procedure for the calculation of thermodynamic properties using this tabular form was described in detail in Refs. [14,15]. The density–temperature plane (ρ, T) is covered with a number of rectangular meshes (ρ_i, T_j), $i = 1, \dots, N_\rho$, $j = 1, \dots, N_T$, that embrace the range of densities and temperatures appearing in the modeling. All the meshes contain the same set of isotherms but can have different sets of isochors. The meshes are constructed so that the phase boundaries (which are the melting, evaporation, and sublimation curves) pass only through the meshes. In such a method of construction, any point corresponding to the stable state lies either inside or on the boundary of a triangular or rectangular cell all of whose corners belong to the region of stability of one and the same phase state. The value of the chosen thermodynamic parameter at an arbitrary point (ρ, T) is found by bilinear (in the case of rectangular cell) or linear (triangular cell) interpolation over the corners of the cell in which this point is situated. The phase diagram of EOS2 is represented in Fig. 3.

To describe the properties of superheated liquid, supercooled vapor, as well as metastable crystal and metastable solid–liquid mixture at negative pressures (EOS3), we calculate additional tables of thermodynamic parameters in the density–temperature plane. The metastable regions are covered by rectangular meshes (X_i, T_j) in the (X, T) plane, where T_j is the same set of isotherms as in the stable case (EOS2), X_i is the set of relative specific volumes determined by the boundaries of metastable regions. For example, the region of existence of metastable vapor is limited by the binodal and spinodal lines; therefore, the X parameter for this region at a given specific volume $V = 1/\rho$ and temperature T is defined as

$$X(V, T) = \frac{V - V_b(T)}{V_{sp}(T) - V_b(T)}, \quad (6)$$

where $V_b(T)$ and $V_{sp}(T)$ are the specific volumes of metastable vapor at the binodal and spinodal at temperature T (below a critical point). The thermodynamic parameters at the arbitrary point (V, T) of a metastable region are then determined by bilinear interpolation using (X, T) variables after $V \rightarrow X$ transformation. The continuity of thermodynamic parameters at transition from stable to metastable region is achieved by the same set of isotherms for meshes divided by phase boundaries.

The chosen interpolation technique provides good merging of thermodynamic surfaces along phase boundaries and guarantees the monotonic behavior of thermodynamic parameters near phase boundaries.

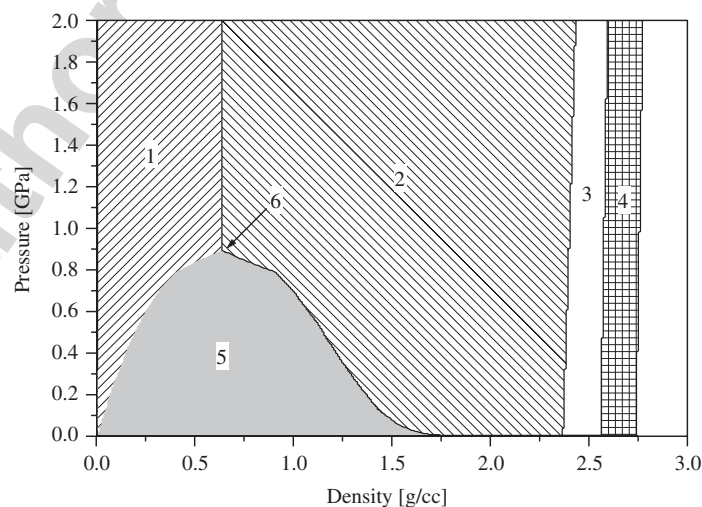


Fig. 3. Phase plane of the temperature complete stable equation of state of aluminum. Phase states are as follows: gas (1), liquid (2), melting region (3), solid (4), and liquid–gas mixture (5). Boundary between phases (1) and (2) with the critical point (6) is conventional.

To calculate thermodynamic properties at a given internal energy and density, we use reverse interpolation. At first, we determine the temperature value and then compute other parameters with the help of direct interpolation as described above.

Earlier [14–16], we have successfully applied the EOSs EOS2 and EOS3 for the simulation of electrical explosion of thin aluminum and tungsten wires.

5. Numerical results

To clarify our results, the same scales of time, distance, and velocity in the computer 2D cylindrical symmetry calculations are used as in the real experiment [17]. The parameters are as follows: impactor diameter is 1.5 cm, target plate thickness is 6.35 mm and impactor velocity is 6.6 km/s. The numerical domain was 30 cm lengthwise and 7.5 cm in the radial direction. The finest computational cell size in our calculations was 0.375 mm.

In Fig. 4, results of the laboratory experiment at 30 μ s after the collision are presented.

It should be noted that the actual plane thickness differs from that apparently shown in the X-ray.

Analysis of the X-ray image highlights several interesting effects of hypervelocity ball-plate interaction. One can see the backsplash, flared at the edges and filaments of material (possibly caused by the action of surface tension force), streaming from fractures at the edges of the hole and ending in a “collar” (dense ring in the widest cross section of the debris cloud, see Fig. 4) at the rear of the cloud. Although laboratory experiment contains information about integral mass distribution projected onto the X-ray we advisedly present the longitudinal section of the cloud to show information about its internal structure.

A plot at 30 μ s of the debris cloud for a simulation using EOS1 is shown in Fig. 5. When the shock wave reached the free surface of the plate, evaporation of lead took place in a strong rarefaction wave. Evaporated matter formed the expanding layer of strongly rarefied gas ($\rho \sim 10^{-5}$ g/cc) moved ahead of leading shell of the cloud. Similar rarefied gas filled the hole and internal volume of backsplash. Numerous fragments consisting of impactor material were formed by reinforcing rarefaction waves.

Numerical modeling with EOS2 demonstrated substantial qualitative differences from EOS1 as shown in Fig. 6. Shock wave propagation along the target plate was accompanied by intensive evaporation from its free surfaces. Spallation did not take place (recall that only positive pressures are allowed in EOS2) and tension zones were filled by two-phase liquid–gas mixture. Also one would not expect the plate target to experience the intensive evaporation from free surfaces in the vicinity of the hole edges due to shock wave propagation although this is seen in the simulation.

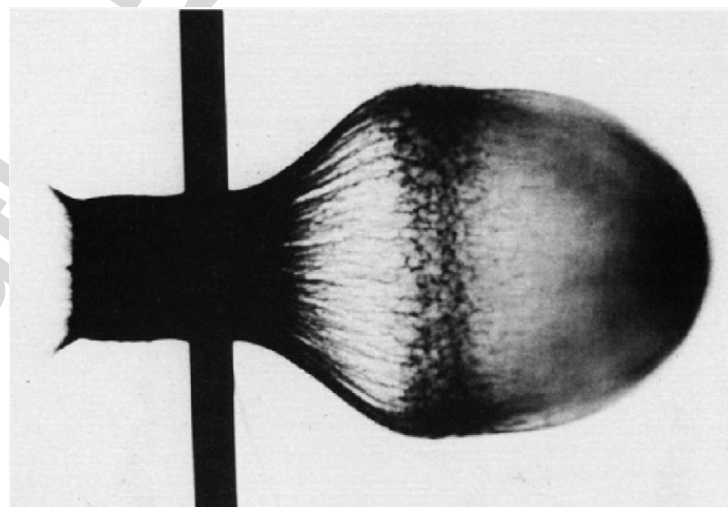


Fig. 4. Experimental X-ray photograph [17] of the lead-on-lead debris cloud (side view). Initially, the Pb ball had a diameter of 1.5 cm and was traveling toward the Pb plate of 6.35 mm thickness from the left at 6.6 km/s. The front of the cloud at 30 μ s is approximately 20 cm away from the plate; the darkest regions indicate the highest densities.

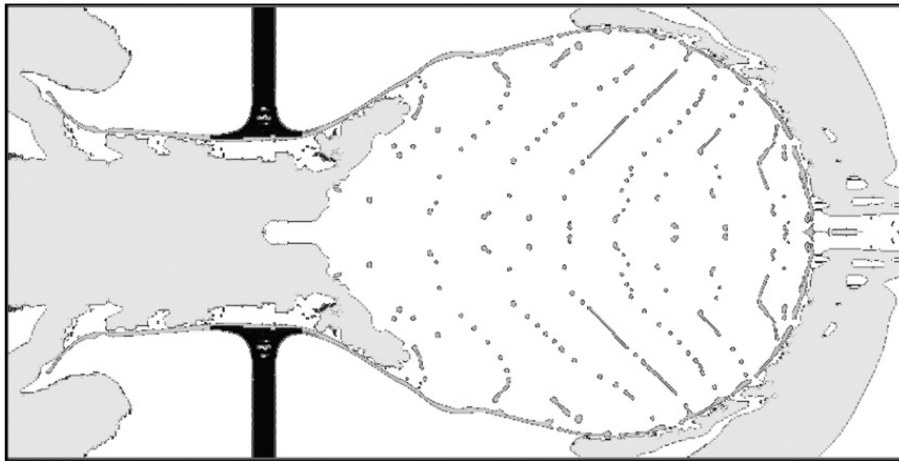


Fig. 5. Calculation with EOS1 for lead at 30 μ s. Numerous fragments form the inner structure of the cloud. Flying back jets are forming the backslash. Gray areas ahead of the cloud shell and inside the backslash represent very rarefied gas at densities near 10^{-5} g/cc.

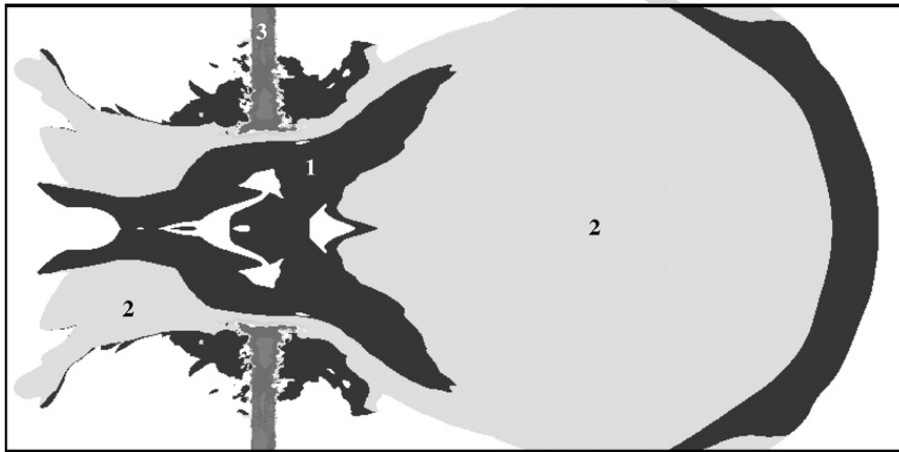


Fig. 6. Calculation with EOS2 for lead. Phase distribution at 30 μ s: gas phase (1), liquid–gas mixture (2), and solid state (3).

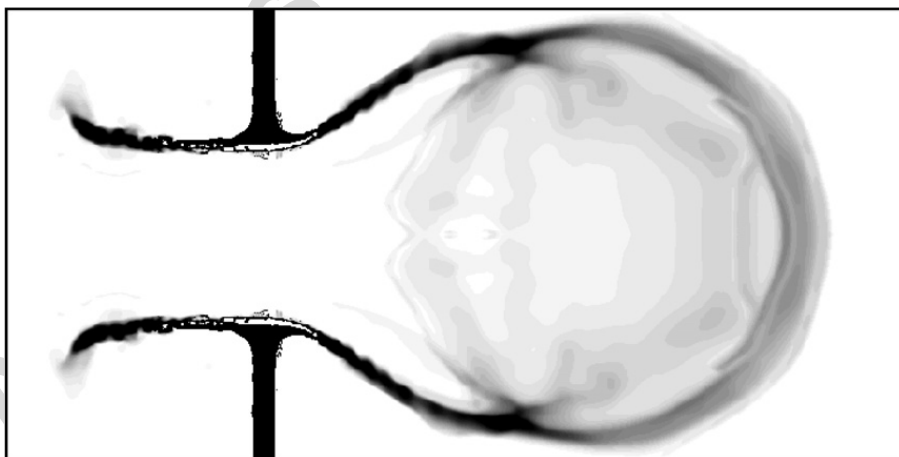


Fig. 7. Calculation with EOS3 for lead at 30 μ s. Density distribution normalized on an interval from 0.01 to 2 g/cc.

The results obtained with EOS3 (see Fig. 7) appear to be closer to those obtained with EOS2 rather than with EOS1. Some differences were observed in the dynamics of the impactor rarefaction stage when the heated projectile started to spall. This process was accompanied by the appearance of void zones in the metastable

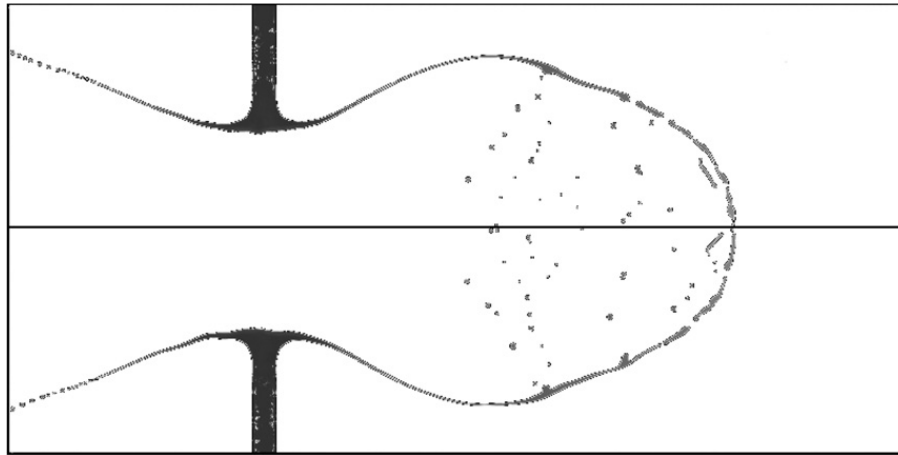


Fig. 8. Calculation with EOS1 (upper half) and EOS3 (lower half) for aluminum at 30 μ s. Density distribution normalized on an interval from 10^{-6} to 3 g/cc.

liquid phase. However, the vacuum cavities lifetime was approximately 4 μ s after which they were filled by evaporated gas fraction. This situation strongly differs from that observed in the case of EOS1 where impactor fragments existed in vacuum during the entire simulation time.

We performed additional simulations to investigate the behavior of other materials under hypervelocity impact loading with different types of EOSs. We used aluminum impactor and target plate (instead of lead) with initial parameters as outlined above. In this case, it was found that there was no difference observed for numerical results obtained with EOS1 and EOS3, see Fig. 8. The reason for such behavior is the greater evaporation energy required for aluminum.

6. Discussion

Lead is a very interesting material for the study of hypervelocity impact problems since it possesses relatively low melting and evaporation temperatures and thus experiences phase transitions under hypervelocity impact. For this reason, it was possible to obtain a wide variety of physical effects in laboratory experiments. We tried to simulate the inner structure of the debris cloud and found a balance between the processes of spallation and evaporation at very high deformation velocities. For example, spall fracture experiments [4] with aluminum and magnesium showed steep drop in the spall strength of preheated samples as temperatures approached the melting point. Comparison of experimental X-ray photographs with results of numerical simulation demonstrates good agreement with the shape and size of debris cloud, flared at the edges backsplash and even the diameter of the hole. Analysis of the numerical simulation results highlights some effects observed in the X-ray. The effect of backsplash flare is explained by cumulation caused by interaction of spherical and flat surfaces so that leading end of jets has different orientation in comparison with the rest of jets.

Formation of the “collar” in numerical simulation has been observed as in the laboratory experiments. The “collar” consists of impactor and plate pieces, which have equal velocities after the rarefaction to zero pressure.

Differences in the structure of clouds were observed in their internal material distribution. To obtain a closer resemblance with experimental data, a model of crack growth should perhaps be taken into account.

7. Conclusions

The computer simulations show that cloud shape is similar to experimental images for all types of EOSs. Agreement has been achieved for material distribution in backsplash, “collar,” and frontal zone.

Modeling with the thermodynamically complete metastable EOS3 gave better agreement with experimental data. The moment of matter spallation depends on lifetimes of metastable phases; therefore, kinetic models ought to be the part of the numerical algorithm.

These conclusions are obtained from the high-order multi-material Godunov method, and they are in good agreement with the results observed in the real experiments [17]. In particular, the hypervelocity impact experiments show that maximal fragmentation is observed using the caloric EOS1. We explain this fact by the conservative value of the bulk sound speed in the vicinity of the cold curve at intermediate densities. On the other hand, the multi-phase EOSs (EOS2, EOS3) include melting and evaporation processes and thus give more accurate values of thermodynamic parameters over a wide range of parameters from highly compressed matter to hot gas fraction.

Acknowledgments

The authors thank Dr. I.N. Lomov for helpful discussions. This work was supported by the Russian Foundation for Basic Research (project No. 06-02-17464) and the Council on Grants from the President of the Russian Federation (project No. NSh-3683.2006.2).

References

- [1] Corbett GG, Reid SR, Johnson W. Impact loading of plates and shells by free-flying projectiles: a review. *Int J Impact Eng* 1997;20:141–230.
- [2] Curran DR, Seaman L. Dynamic failure of solids. *Phys Rep* 1987;147:253–388.
- [3] Mescheryakov YI, Mahutov NA, Atroshenko SA. Micromechanisms of dynamic fracture of ductile high-strength steels. *J Mech Phys Solids* 1994;42:1435–57.
- [4] Kanel GI, Razorenov SV, Bogatch A, Utkin AV, Grady DE. Simulation of spall fracture of aluminum and magnesium over a wide range of load duration and temperature. *Int J Impact Eng* 1997;20:467–78.
- [5] Miller GH, Puckett EG. A high-order Godunov method for multiple condensed phases. *J Comput Phys* 1996;128:134–64.
- [6] Henderson LF, Colella P, Puckett EG. On the refraction of shock waves at a slow-fast gas interface. *J Fluid Mech* 1991;224:1–27.
- [7] Van Leer B. Towards the ultimate conservative difference scheme, a second order sequel to Godunov's method. *J Comput Phys* 1979;32:101–36.
- [8] Colella P, Glaz HM. Efficient solution algorithm for the Riemann problem for real gases. *J Comput Phys* 1985;54:264–89.
- [9] Pilliod JE, Puckett EG. Second-order accurate volume-of-fluid algorithms for tracking material interfaces. *J Comput Phys* 2004;199:465–502.
- [10] Chorin JA. Random choice methods with applications to reacting gas flow. *J Comput Phys* 1977;25:253–72.
- [11] Dukowicz JK. A general, non-iterative Riemann solver for Godunov's method. *J Comput Phys* 1985;61:119–37.
- [12] Khishchenko KV. The equation of state for magnesium at high pressures. *Tech Phys Lett* 2004;30:829–31.
- [13] Bushman AV, Kanel GI, Ni AL, Fortov VE. Intense dynamic loading of condensed matter. Washington, DC: Taylor and Francis; 1993.
- [14] Tkachenko SI, Khishchenko KV, Vorob'ev VS, Levashov PR, Lomonosov IV, Fortov VE. Metastable states of liquids metal under conditions of electric explosion. *High Temp* 2001;39:674–87.
- [15] Oreshkin VI, Baksht RB, Ratakhin NA, Shishlov AV, Khishchenko KV, Levashov PR, et al. Wire explosion in vacuum: simulation of a striation appearance. *Phys Plasmas* 2004;11:4771–6.
- [16] Khishchenko KV, Tkachenko SI, Levashov PR, Lomonosov IV, Vorob'ev VS. Metastable states of liquid tungsten under subsecond wire explosion. *Int J Thermophys* 2002;23:1359–67.
- [17] Holian BL. Hypervelocity-impact phenomena via molecular dynamics. *Phys Rev A* 1987;36:3943–6.